Parameter-Independent Battery Control Based on Series and Parallel Impedance Emulation

Andoni Urtasun[1], Member, IEEE, Pablo Sanchis[1], Senior Member, IEEE, Francesc Guinjoan[2], Member, IEEE, and Luis Marroyo[1], Member, IEEE

[1]Department of Electrical, Electronic and Communications Engineering, Public University of Navarre, Spain
[2]Department of Electronics Engineering, Universitat Politècnica de Catalunya, Barcelona, Spain

Corresponding author: Andoni Urtasun (e-mail: andoni.urtasun@unavarra.es).

ABSTRACT Appropriate voltage control is essential in order to extend the useful life of a battery. However, when universal chargers are used, the design of this control becomes more complicated, given the fact that the battery impedance value may vary considerably, depending not only on the operating point but also on the type, size and aging level of the battery. This paper firstly shows how the voltage regulation can become extremely variable or even unstable when the controller is designed according to the proposals in the literature. We then go on to propose the emulation of a series and parallel impedance with the battery, which is easy to implement and achieves a control that is completely independent of the battery connected. The simulation results obtained for batteries with resistances ranging from 10 mΩ to 1 Ω, show the problems with existing controls and confirm that the proposed control response is similar for all the possible range of battery resistances.

INDEX TERMS Battery charger, battery management, robust control, virtual impedance emulation, voltage control.

I. INTRODUCTION

Energy storage is becoming increasingly important as a result of the massive growth in e-mobility and renewable energy systems [1], [2]. Of the different storage technologies available, batteries are the most common thanks to their high efficiency, energy density and low cost, and are used in range of applications such as e-vehicles [3], [4], power regulation at PV plants and wind farms [5]–[7], stand-alone systems [8], [9] and microgrids [10], [11].

In these systems, batteries form a significant part of the total cost and it is therefore advantageous to maximize their useful life [12], [13]. Of the different factors affecting battery degradation, the incorrect charge induces the rapid build-up of internal stress and resistance, and other negative effects [14]–[16]. In particular, over-charging results in undesirable chemical and electrochemical reactions and greatly reduces cycle life, as reported for example in [17] and [18] for lithium-ion batteries and in [19] for lead-acid batteries. For this reason, it is essential to ensure a correct charge through the electronic converter connected to the battery. Although there are a number of algorithms to do so, the most common are: Constant-Current (CC)-Constant-Voltage (CV) charging

for lithium-ion batteries [20], and Three Stage Charging (TSC) for lead-acid [21], [22], and flow batteries [23], [24].

In both cases, there are two principle stages, depending on whether the battery voltage or current is to be regulated. In CC mode, the battery current is controlled to a given value if power is available (for example when charging an e-vehicle) or under the said value, depending on the availability of the resource and the energy management strategy (for example in a stand-alone system or microgrid). Once the battery is charged, the control switches to CV mode, whereby the battery charger regulates the voltage so that the current is progressively reduced [20]–[24].

In order to apply this charging process, the electronic converter connected to the battery must be able to regulate both the current and the voltage, and also to smoothly switch from one mode to the other. For this purpose, principally two control strategies can be found in the literature, as shown in Fig. 1. For the first one, Fig. 1(a), the current and voltage are regulated independently by two simple loops. The charge mode selector is responsible for selecting what control voltage to apply, depending on whether the system is in CC or CV mode [25]–[27]. For the second strategy, Fig. 1(b), a

cascaded control is implemented, whereby the current is regulated in the inner loop. As shown in the figure, the current reference is obtained as the minimum between two values. When the system is in CC mode, the battery voltage is lower than its reference voltage so that $I^*_{bat,CV}$ reaches saturation at a high value and $I^*_{bat,CC}$ is selected. On the contrary, when the battery voltage exceeds the reference voltage, then the value of $I^*_{bat,CV}$ is reduced and is selected to regulate the battery voltage [28]–[32].

a) Two single feedback loops
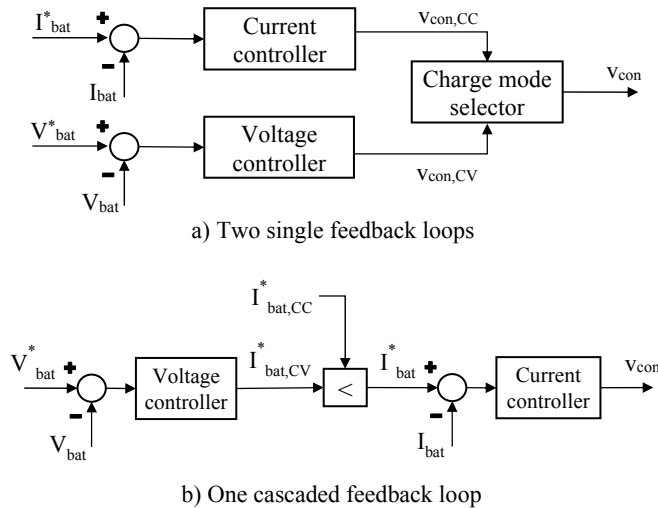
b) One cascaded feedback loop

FIGURE 1. Battery voltage and current regulations: a) two single feedback loops, b) one cascaded feedback loop.

With the exception of low power applications, the second option is preferable given that the current is always protected, making it possible to extend the useful life of the battery and the converter. However, with this strategy, the voltage loop becomes highly dependent on the battery impedance. The problem is that this impedance is normally unknown and difficult to estimate given that, when the control is implemented in a universal charger, the latter could be connected to batteries of a different technology with a different capacity and number of cells in series/parallel. A further complication is that this impedance is also highly variable as a function of the operating point, including state of charge, state of health, temperature and even the level of current. In view of all this, it would be ideal to design a robust voltage control to cover a wide range of battery impedances [33], [34].

Despite these problems, the voltage control is generally designed for a specific impedance, without taking into account the effect of impedance variation on this control [26], [28]–[30], [35], [36]. However, as will be shown in this paper, this causes the voltage loop dynamics to be extremely variable, based on the type of battery connected, and may even become unstable in certain circumstances.

This variation in dynamics may be serious in some applications, for example in the case of a stand-alone system with renewable energy sources. In this system, the

switch from CC mode to CV mode may be abrupt as a result of an increase in the resource or due to load disconnection, which could lead to overvoltage in the battery [9], [35], [37]. Therefore, in order to lessen the damage to the battery, it is important to get a rapid response from the voltage loop, regardless of the type of battery connected.

In order to achieve a controller that is immune to variations in parameters, nonlinear controllers have been proposed in the literature. In [27], the battery voltage is regulated by hysteresis control, obtaining a more robust regulation but at the expense of having a variable switching frequency and low noise immunity. In [31] and [32], the authors propose estimating the battery resistance and using the estimation in an adaptive control. The problem with this method is that the estimation algorithm considerably increases the computational cost. In [38], the battery voltage is controlled by fuzzy logic. In this case, the parameters must be experimentally tuned and the robustness of the controller is not guaranteed [39].

To overcome the disadvantages of these methods, in [40] a linear control is proposed, with a low computational cost and based on the emulation of an impedance in parallel with the battery. With this method, it is possible to reduce the variability of the control to a large extent. However, the virtual impedance design proposal cannot be generalized, given that it is based on approximations made on the inner current loop and on digitization, which considerably limit its applicability and may result in an unstable control. Moreover, the resistance emulated has a very low value, which decreases noise immunity and could cause undesired saturations.

This article proposes the emulation of series and parallel impedances. This solution is very simple to implement and achieves full robustness, with no control variability whatsoever. Moreover, it is not necessary to emulate very small resistances, considerably improving immunity to noise.

This paper is organized as follows. Section II presents the system analyzed, including the model used for the battery. In section III, the model for the inner current loop is obtained, taking into account the influence of the battery resistance. Then, in section IV, an analysis is made of the voltage regulation for three different controls: firstly, the traditional control with an integral controller; secondly, the method with parallel impedance emulation, showing that the control design proposed in [40] would lead to an unstable control for the case study of this paper, and then proposing an improved parallel impedance design; thirdly, the proposed method with series and parallel impedance emulation. The simulation results for all three methods are shown in section V and, finally, the conclusions of the study are set out in section VI.

II. SYSTEM DESCRIPTION

The system studied consists in a battery connected to a boost converter which functions as a charger, as shown in Fig. 2. In general, the device connected to the output varies with the application, and could be a voltage-fed inverter or the DC bus of an e-vehicle, for example. In any case, the main application of universal chargers is to be combined with a single-phase inverter for grid-connected or off-grid ac systems, a solution which is offered by many converter manufacturers. The charger specifications are shown in Table I, where it can be seen that it is valid for different types of batteries and voltage levels.
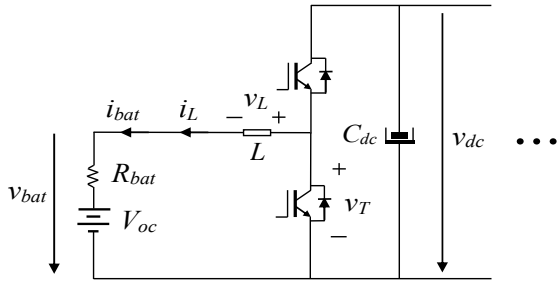

FIGURE 2. Battery connected to a boost converter charger.

TABLE I
SPECIFICATIONS OF THE BOOST CONVERTER CHARGER

Battery chemistry	Lithium-ion, lead-acid, flow
Nominal battery voltage	Between 48 and 240 V
Output voltage V_{dc}	350 V
Converter rated current	50 A
Converter inductor L	750 µH
Voltage control sampling time T_{sv}	1 ms
Time constant of the voltage filter, τ_v	53 µs
Current control sampling time T_{si}	125 µs
Time constant of the current filter, τ_i	53 µs
Converter switching frequency	16 kHz

Various battery models can be found in the literature, which are used for different purposes such as control design, state-of-charge and state-of-health calculation, online parameter estimation… [41], [42]. In the case of control design, a dynamic model should be employed, which usually considers an open circuit voltage source V_{oc} in series with an internal resistor and one or more RC branches [30], [35], [43]–[45]. For clarity in the control design, in this paper total impedance of the battery, Z_{bat}, is first approximated to resistance R_{bat}. Then, in order to assess stability, a robustness analysis is later carried out with a more accurate model. Thus, in small signal, the battery impedance can be expressed as

$$Z_{bat}(s) = \frac{\hat{v}_{bat}}{\hat{i}_{bat}} = \frac{\hat{v}_{bat}}{\hat{i}_L} \approx R_{bat}. \qquad (1)$$

Since the control is implemented in the universal charger, and the type of battery to be connected is unknown, an extremely wide range of possible resistances must be considered, taking into account the influence of the battery type, its capacity, the number of cells in series, its operating point and its aging level. In the search made in [40], it was concluded that the variation range for this charger could be between $R_{bat,min}$ = 10 mΩ (new lithium-ion battery with a low rated voltage, high current and operating at a high temperature) and $R_{bat,max}$ = 1 Ω (used lead acid battery with a high rated voltage, low capacity and operating at a low temperature) [46]–[50]. This 100 times variation range will also be the one considered in this study.

III. MODELING OF THE INNER CURRENT LOOP

In CV mode, the voltage regulation which employs a cascaded feedback loop is used here [see Fig. 1 (b)], as it offers some advantages for this application [31]. Since the battery current is regulated in the inner loop, this control is analyzed first.

Considering average values in a switching period, from Fig. 2, the inductor voltage v_L can be determined as

$$v_L = L \cdot \frac{di_L}{dt} = v_T - v_{bat} = d \cdot v_{dc} - v_{bat}, \qquad (2)$$

where d is the duty cycle of the upper transistor.

As can be observed in (2), both input and output voltages, v_{bat} and v_{dc}, affect the current. Thus, in order to reduce the influence of input and output impedances on the current control, measured variables $v_{bat,f}$ and $v_{dc,f}$ are used as feedforward compensation, leading to the inductor current loop shown in Fig. 3, where i^*_L is the reference inductor current, v^*_L the reference inductor voltage, v^*_T the reference switch voltage, $i_{L,f}$ the measured inductor current, C_i represents the current controller, S_i the sampling and computation delay, H_v the voltage sensing and H_i the current sensing.

The sensing transfer functions are modeled as

$$H_i(s) = \frac{1}{\tau_i \cdot s + 1}, \quad H_v(s) = \frac{1}{\tau_v \cdot s + 1}, \qquad (3)$$

where τ_i and τ_v are the time constants of the inductor current and battery voltage sensing, respectively.
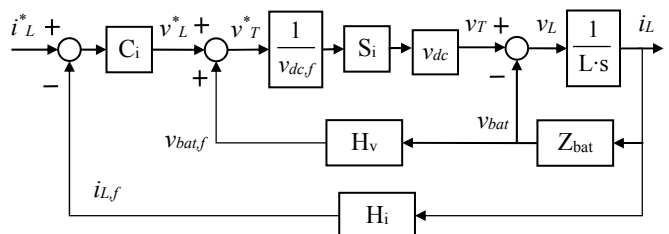

FIGURE 3. Model of the inductor current control loop.

For transfer function S_i, the zero-order hold and the computation delay must be considered, which can be modeled as

$$S_i(s) = \frac{1 - 0.5 \cdot T_{si} \cdot s}{(1 + 0.5 \cdot T_{si} \cdot s)^2} \cdot \qquad (4)$$

where T_{si} is the sampling time and the approximation is accurate up to $f \approx 1/(4 \cdot T_{si})$ [51].

As a large capacitor is usually placed at the dc bus, it is possible to assume that the dc voltage compensation is ideal [52]. As a result, from Fig. 3, the plant seen by the current controller, Y_{eq}, can be obtained as

$$Y_{eq}(s) = \frac{i_L}{v_L^*} = \frac{S_i}{L \cdot s + Z_{bat} \cdot (1 - H_v \cdot S_i)} \cdot \qquad (5)$$

Due to the low battery impedance values, the current regulator, a PI controller, can be designed assuming that $Z_{bat} = 0$ and thus $Y_{eq} = S_i/Ls$. For this plant, the parameters are tuned for a crossover frequency $f_{ci} = 450$ Hz and a phase margin $\Phi_{mi} = 47°$.

From Fig. 3 and considering (5), the closed-loop transfer function for the current control can be determined as

$$G_{icl}(s) = \frac{i_L}{i_L^*} = \frac{C_i \cdot Y_{eq}}{1 + C_i \cdot Y_{eq} \cdot H_i} \cdot \qquad (6)$$

The Bode plot of G_{icl} is represented in Fig. 4 for three different battery resistances, namely $R_{bat,min} = 10$ mΩ, $R_{bat,med} = 100$ mΩ and $R_{bat,max} = 1$ Ω. As can be observed, although the battery influence is modest, the current closed-loop is more damped for $R_{bat,max} = 1$ Ω.
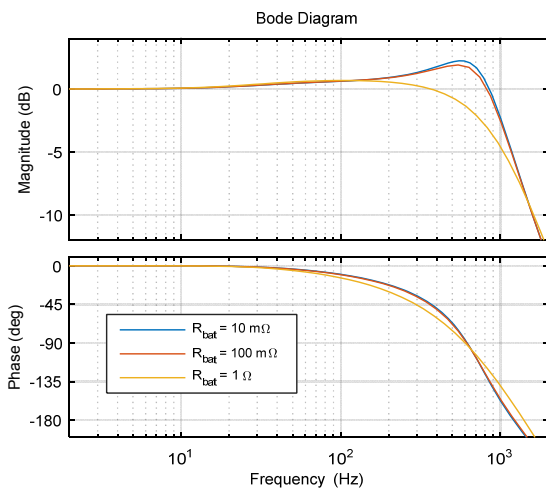

FIGURE 4. Current closed-loop G_{icl} for three different battery resistances (R_{bat} = 10 mΩ, R_{bat} = 100 mΩ and R_{bat} = 1 Ω).

IV. VOLTAGE REGULATION

A. TRADITIONAL CONTROL
The traditional battery voltage control loop is shown in Fig. 5, where v_{bat}^* is the reference battery voltage, C_v

represents the voltage controller, z^{-1} the computation delay and *ZOH* the zero-order hold.
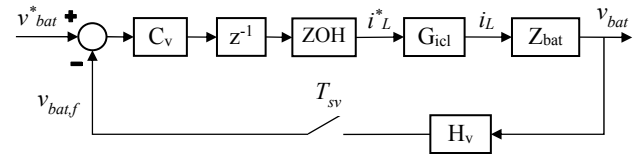

FIGURE 5. Traditional control loop for the battery voltage.

In contrast to the current loop model, the continuous approximation is not applied in the voltage control since it is important to obtain an accurate model around the Nyquist frequency, as will become clear in the following sections. From Fig. 5, the open-loop transfer function can be determined as

$$OL(z) = C_v \cdot z^{-1} \cdot Z_{vf}, \qquad (7)$$

$$Z_{vf}(z) = \frac{v_{bat,f}(z)}{i_L^*(z)} = (1 - z^{-1}) \cdot \mathbb{Z} \left\{ \frac{G_{icl} \cdot Z_{bat} \cdot H_v}{s} \right\} \cdot \qquad (8)$$

The voltage regulator employed is the discrete equivalent of an integral controller by using Tustin's method. Its expression in the z-domain is

$$C_v(z) = \frac{K_i \cdot T_{sv}}{2} \frac{z + 1}{z - 1} \cdot \qquad (9)$$

Integral gain K_i is usually calculated for a certain battery resistance, without taking into account its variation range. In this case, the resistance is considered as the geometric mean between $R_{bat,min} = 10$ mΩ and $R_{bat,max} = 1$ Ω, that is $R_{bat,med} = 100$ mΩ. According to the battery characteristics, a low crossover frequency is required for the voltage regulation, and it is set to $f_c = 0.5$ Hz.

Figure 6 shows the Bode plot of the compensated open loop for three different battery resistances, pointing out the crossover frequency and phase margin. As can be observed, for $R_{bat,med} = 100$ mΩ, the voltage response is as designed, with $f_c = 0.5$ Hz. However, it slows down to $f_c = 0.05$ Hz for $R_{bat,min} = 10$ mΩ and speeds up to $f_c = 5$ Hz for $R_{bat,max} = 1$ Ω. In short, depending on the battery, the control can be too far from the desired performance and is not suitable for some applications such as renewable energy-based stand-alone systems.

B. PARALLEL IMPEDANCE EMULATION
In order to reduce the control variability, the emulation of an impedance in parallel with the battery is proposed in [40]. The implementation of this virtual impedance can be observed in the control scheme shown in Fig. 7, where Y_p is the virtual parallel admittance, Z_p the virtual parallel impedance, i_{Zp} the current through that impedance, and i_v the virtual current.
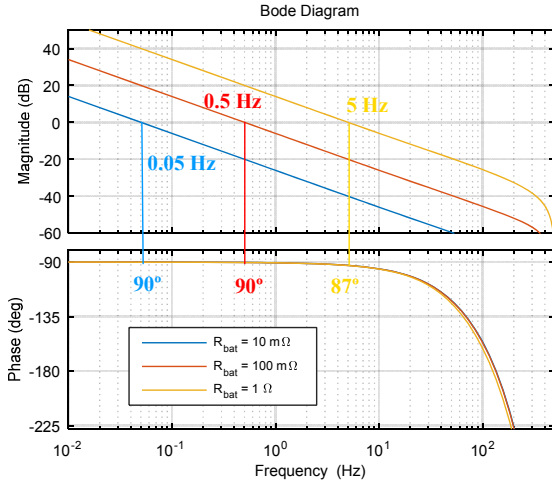
FIGURE 6. Compensated open-loop for the traditional control, for three different battery resistances (R_{bat} = 10 mΩ, R_{bat} = 100 mΩ and R_{bat} = 1 Ω).
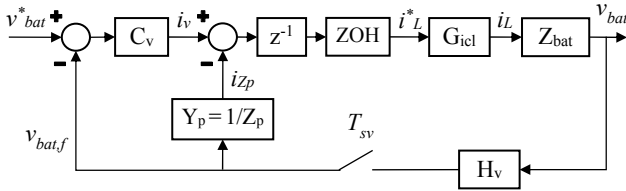

FIGURE 7. Battery voltage control loop for the parallel impedance emulation.

As a result of the impedance emulation, the equivalent impedance seen by the controller, Z_{eq}, is modified and becomes (10), i.e. the parallel between Z_p and z^{-1}·Z_{vf}, where Z_{vf} was defined in (8). Thus, if the virtual impedance Z_p is small enough around the frequencies of concern, the system would behave as this known impedance and the plant variability would be compensated.

$$Z_{eq}(z) = \frac{v_{bat,f}(z)}{i_v(z)} = \frac{z^{-1} \cdot Z_{vf}}{1 + Y_p \cdot z^{-1} \cdot Z_{vf}} = Z_p \, / / \left(z^{-1} \cdot Z_{vf} \right). \quad (10)$$

According to [40], the emulation of an RL impedance is the best solution for this application and, as a rule of thumb, its parameters R_p and L_p can be selected such that $L_p \cdot \omega_c = R_p$, where ω_c is the angular crossover frequency of the voltage regulation. For this impedance, the parallel admittance Y_p in s-domain and its implementation in z-domain using the zero-order hold equivalent, can be expressed as

$$Y_p(s) = \frac{1}{R_p} \cdot \frac{1}{s / \omega_c + 1} \Rightarrow Y_p(z) = \frac{1}{R_p} \cdot \frac{1 - \exp\left(-\omega_c \cdot T_{sv}\right)}{z - \exp\left(-\omega_c \cdot T_{sv}\right)}. \quad (11)$$

As the virtual impedance is located in the feedback path (see Fig. 7), the minimum value of virtual resistance R_p is limited in order to avoid right-half-plane (RHP) poles in the equivalent impedance Z_{eq}. In [40], two conditions for a stable emulation were obtained. When applied to the case study of this paper, these constraints are $R_p >$ 0.160 mΩ and

$R_p > 0.899$ mΩ, leading to $R_p = 2.26$ mΩ and $L_p = 719$ μH, after considering a gain margin of 8 dB. Around $f_c = 0.5$ Hz, this impedance is much smaller than the battery resistance and is thus expected to remove the influence of the battery on the control. However, the stability analysis carried out in [40] is based on several approximations which cannot be applied to this case. Specifically, the voltage loop is an s-domain model, and first-order models are considered for the zero-order hold together with the computation delay and for the current closed-loop.

The improved model developed in this paper can be used to better evaluate the stability of the impedance emulation. For this purpose, the Bode plot of the open-loop transfer function of the emulation, $Y_p \cdot z^{-1} \cdot Z_{vf}$ (see Fig. 7), is represented in Fig. 8 for the virtual impedance designed as proposed in [40]. This figure is plotted for three different battery resistances and the gain margins are highlighted. As can be observed, although the design gain margin for $R_{bat,max} = 1$ Ω was 8 dB, the improved model shows that in reality it is equal to -7.6 dB, so the impedance emulation will be unstable when operating with high battery resistances.
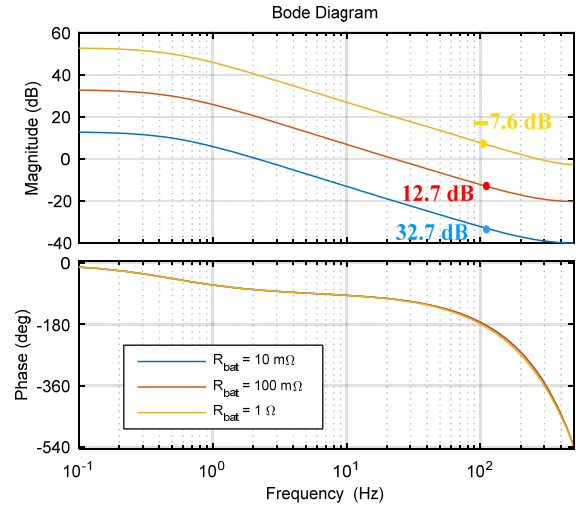

FIGURE 8. Open-loop for the parallel impedance emulation, $Y_p \cdot z^{-1} \cdot Z_{vf}$, designed as proposed in [37], for three different battery resistances (R_{bat} = 10 mΩ, R_{bat} = 100 mΩ and R_{bat} = 1 Ω).

As a result, it becomes clear that the approximations of [40] cannot be always applied and a higher virtual resistance R_p needs to be selected in order to ensure stability. Specifically, $R_p = 13.7$ mΩ is required to obtain a gain margin of 8 dB, which leads to $L_p = 4.35$ mH.

With this virtual parallel impedance, the equivalent impedance seen by the controller can be obtained by means of (10) and is represented in Fig. 9 for three different battery resistances and for the ideal case where $Z_{eq} = Z_p$. As can be observed, thanks to the impedance emulation, the impedance variation at 0.5 Hz is now between 7.1 to 19.1 mΩ, meaning that the plant variability has been reduced from 100 times to 2.7 times.

IEEE *Access*
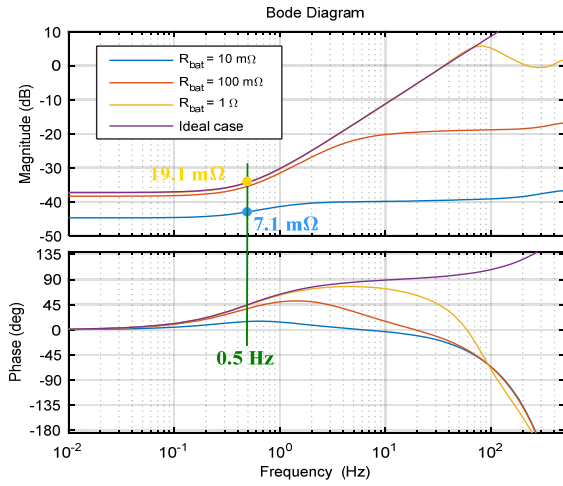Multidisciplinary : Rapid Review : Open Access Journal

FIGURE 9. Equivalent impedance after the parallel impedance emulation, for the ideal case where $Z_{eq} = Z_p$ and for three different battery resistances (R_{bat} = 10 mΩ, R_{bat} = 100 mΩ and R_{bat} = 1 Ω).

Finally, voltage controller C_v is selected in the s-domain as an integrator together with a pole to further reduce the gain at high frequencies. In this case, the digital implementation is not critical so any discrete equivalent can be used. The controller parameters are selected to obtain a minimum phase margin of 60º and a maximum crossover frequency of 0.5 Hz. The Bode plot of the compensated open-loop is shown in Fig. 10 for three different battery resistances, where it can be observed that, for $R_{bat,max} = 1\ \Omega$, the crossover frequency is 0.5 Hz and for $R_{bat,min} = 10$ mΩ, the crossover frequency is 0.24 Hz. Comparing these results with the traditional control response shown in Fig. 6, it is clear that control robustness has been greatly improved.
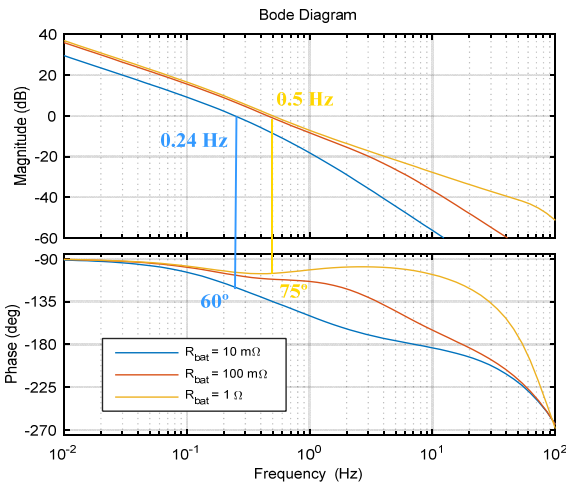

FIGURE 10. Compensated open-loop for the parallel impedance emulation, $C_v \cdot Z_{eq}$, for three different battery resistances (R_{bat} = 10 mΩ, R_{bat} = 100 mΩ and R_{bat} = 1 Ω).

In spite of this improvement over the traditional control, the voltage response is still variable depending on the connected battery. More importantly, this method requires a

very small parallel impedance in order to be effective, which reduces noise immunity and can cause undesired saturations. For example, for the case study, $R_p = 13.7$ mΩ is used, resulting in a virtual current in steady-state which can reach several kA.

C. SERIES AND PARALLEL IMPEDANCE EMULATION

The proposed voltage loop for series and parallel impedance emulation is shown in Fig. 11, where Z_s is the virtual series impedance, v_{Zs} the voltage drop across that impedance and v_v the virtual voltage. From this figure, the equivalent impedance seen by the controller can be obtained as

$$Z_{eq}(z) = \frac{v_{bat,f}(z)}{i_v(z)} = \frac{z^{-1} \cdot Z_{vf}}{1 + Y_p \cdot \left(z^{-1} \cdot Z_{vf} + z^{-1} \cdot G_{if} \cdot Z_s \right)}, \quad (12)$$

$$G_{if}(z) = \frac{i_{L,f}(z)}{i_L^*(z)} = (1 - z^{-1}) \cdot \mathbb{Z}\left\{ \frac{G_{icl} \cdot H_i}{s} \right\}. \quad (13)$$
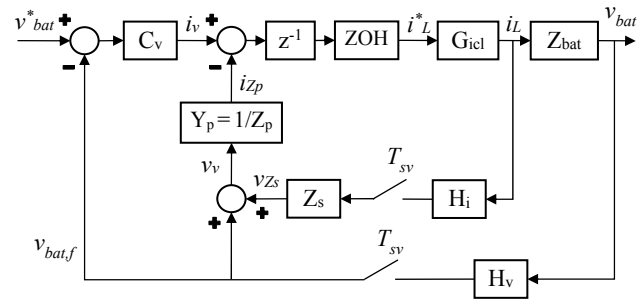

FIGURE 11. Model of the battery voltage control loop for the series and parallel impedance emulation.

At low frequencies, it can be assumed that the sensing filters and current closed-loop are instantaneous, i.e. $H_v = H_i = G_{icl} = 1$, and the ZOH and computation delay can be disregarded. As a result, the equivalent impedance shown in (12) can be approximated as

$$Z_{eq,appox}(s) = \frac{v_{bat}(s)}{i_v(s)} = \frac{Z_p \cdot Z_{bat}}{Z_p + Z_s + Z_{bat}}. \quad (14)$$

The impedance Z_{eq} expressed in (12) and its low-frequency approximation $Z_{eq,approx}$ expressed in (14) can be represented in an equivalent circuit, as shown in Fig. 12(a) and Fig. 12(b), respectively. As can be observed in both figures, an impedance in series with the battery is now combined with the parallel impedance emulated in the previous section.
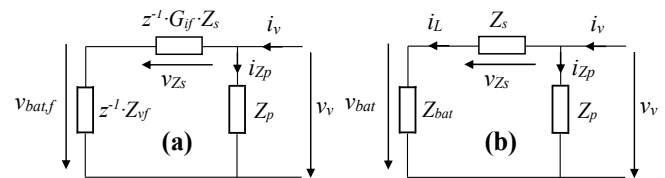

FIGURE 12. Equivalent circuit for the series and parallel impedance emulation: (a) real equivalent circuit, (b) ideal equivalent circuit, valid at low frequencies.

From (14), if series and parallel impedances are emulated in such a way that $Z_s = -Z_p$, the equivalent impedance Z_{eq} becomes completely independent of the battery impedance Z_{bat}. In other words,

$$Z_s = -Z_p \implies Z_{eq,appox}(s) = \frac{v_{bat}(s)}{i_v(s)} = Z_p. \qquad (15)$$

In order to fulfill (15) and for ease of implementation, $Z_p = R$ and $Z_s = -R$ are selected. By means of (12), one must now verify whether virtual resistance R can be tuned to maintain a stable emulation. For this purpose, the Bode plot of the open-loop transfer function, $Y_p \cdot z^{-1} \cdot (Z_{vf} + G_{if} \cdot Z_s)$ is represented in Fig. 13 for $R = 600$ mΩ and for three different battery resistances. As can be observed, for $R_{bat,max} = 1$ Ω, the gain margin is 2.9 dB so the emulation will be stable. Furthermore, this gain margin can be increased by selecting a higher value for virtual resistance R. However, for $R_{bat,med} = 100$ mΩ and $R_{bat,min} = 10$ mΩ, the gain margin at the Nyquist frequency is negative, which means that an RHP pole will appear in equivalent impedance Z_{eq}. It is worth noting that, if a continuous model had been used, this instability would have not been detected.
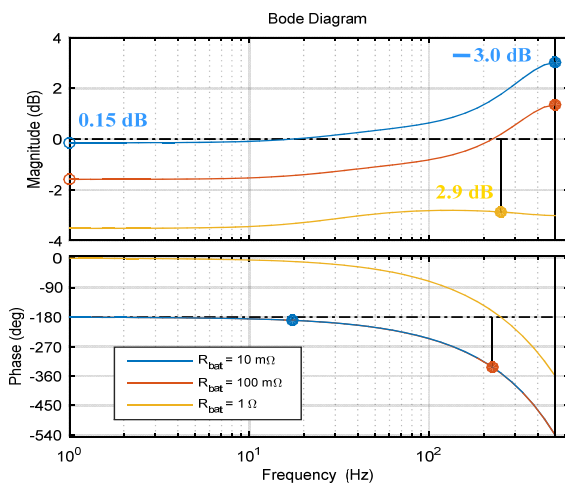

FIGURE 13. Open-loop for the series and parallel impedance emulation, $Y_p \cdot z^{-1} \cdot (Z_{vf} + G_{if} \cdot Z_s)$, with $R = 600$ mΩ, for three different battery resistances ($R_{bat} = 10$ mΩ, $R_{bat} = 100$ mΩ and $R_{bat} = 1$ Ω).

For low battery resistances, the gain margin hardly depends on the virtual resistance R and there is no R value which can provide a stable emulation for the selected virtual impedances. For this reason, whereas the series impedance is maintained as $Z_s = -R$, the parallel impedance Z_p is modified so that a low-pass filter is introduced in the open loop transfer function, $Y_p \cdot z^{-1} \cdot (Z_{vf} + G_{if} \cdot Z_s)$, making it possible to reduce the gain at Nyquist frequency. Specifically, parallel admittance Y_p is implemented as

$$Y_p(z) = \frac{1}{R} \cdot \frac{1 + z^{-1}}{2}. \qquad (16)$$

By using this series and parallel emulation with $R = 687$ mΩ, the Bode plot of the open-loop transfer function, $Y_p \cdot z^{-1} \cdot (Z_{vf} + G_{if} \cdot Z_s)$ is represented in Fig. 14 for three different battery resistances. As can be observed in the figure, all gain margins are now positive, resulting in a stable emulation. Although it may seem that the 0-Hz gain margin is too low, in reality it does not change when modifying the system parameters, so it is high enough.
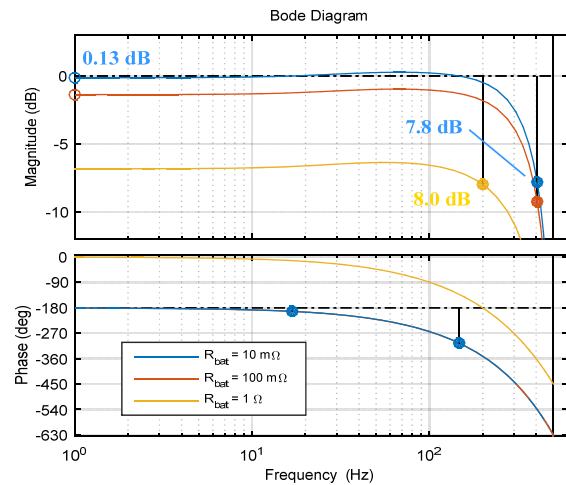

FIGURE 14. Open-loop for the series and parallel impedance emulation, $Y_p \cdot z^{-1} \cdot (Z_{vf} + G_{if} \cdot Z_s)$, with $R = 687$ mΩ and low-pass filter, for three different battery resistances ($R_{bat} = 10$ mΩ, $R_{bat} = 100$ mΩ and $R_{bat} = 1$ Ω).

Once the impedance emulation is designed, the equivalent impedance seen by the controller can be obtained by means of (12) and is represented in Fig. 15 for three different battery resistances and for the ideal case where $Z_{eq} = Z_p$. Thanks to the proposed method, the impedance variation at 0.5 Hz has completely disappeared.
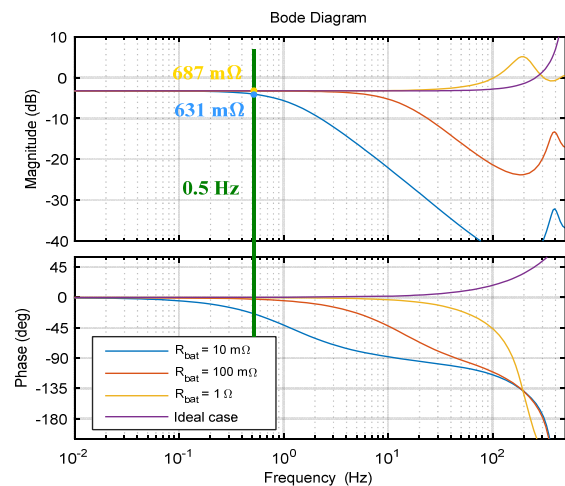

FIGURE 15. Equivalent impedance after the series and parallel impedance emulation, for the ideal case where $Z_{eq} = Z_p$ and for three different battery resistances ($R_{bat} = 10$ mΩ, $R_{bat} = 100$ mΩ and $R_{bat} = 1$ Ω).

Voltage controller C_v is chosen as an integral controller, implemented as shown in (9), and tuned for a crossover

frequency of 0.5 Hz. Figure 16 shows the Bode plot of the compensated open-loop for three different battery resistances. As can be observed, the crossover frequency varies between 0.47 and 0.5 Hz, meaning that the effect of the battery resistance on the control has been completely removed.
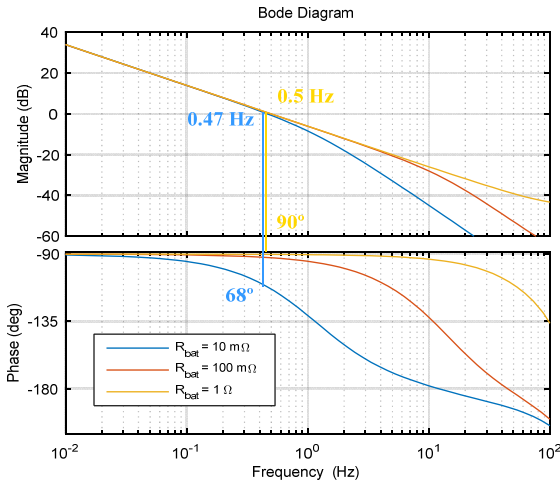

FIGURE 16. Compensated open-loop for series and parallel impedance emulation, $C_v \cdot Z_{eq}$, for three different battery resistances (R_{bat} = 10 mΩ, R_{bat} = 100 mΩ and R_{bat} = 1 Ω).

D. ROBUSTNESS ANALYSIS

Up to this point, the battery impedance has been modeled as a pure resistance R_{bat}. However, in the frequencies of concern, between 0.2 and 500 Hz, the battery dynamic behavior can be more accurately described by a resistance in series with an RC branch [44]. This battery impedance can be expressed as

$$Z_{bat}(s) = \frac{\hat{v}_{bat}}{\hat{i}_{bat}} = \frac{\hat{v}_{bat}}{\hat{i}_L} \approx \frac{C_{dl} \cdot r_c \cdot r_0 \cdot s + r_0 + r_c}{C_{dl} \cdot r_c \cdot s + 1}, \quad (17)$$

where r_0 is the ohmic resistance, r_c the charge transfer resistance and C_{dl} the double-layer capacitor.

Since this transfer function is equivalent to a lag compensator, it can also be defined as

$$Z_{bat}(s) = \frac{\hat{v}_{bat}}{\hat{i}_{bat}} = \frac{\hat{v}_{bat}}{\hat{i}_L} \approx R_{bat} \cdot \frac{\alpha \cdot \tau \cdot s + 1}{\tau \cdot s + 1}, \quad (18)$$

$$R_{bat} = r_0 + r_c, \quad \alpha = \frac{r_0}{r_0 + r_c}, \quad \tau = C_{dl} \cdot r_c \cdot \quad (19)$$

By means of this model, a robustness analysis is carried out for the variation of the three parameters defined in (19), where R_{bat} is delimited between 10 mΩ and 1 Ω, and α between 0.5 and 0.8.

To study the stability of the parallel impedance emulation presented in section IV.B, the Bode plot of the open-loop transfer function of the emulation, $Y_p \cdot z^{-1} \cdot Z_{vf}$ [see (10) and Fig. 8], should be evaluated. This transfer function is represented in Fig. 17 for R_{bat} = 1 Ω and different

situations, including the resistive battery model used for the control design, and the dynamic model presented here for α = 0.6 and τ varying from 0.4 to 400 ms. As can be observed, the minimum gain margin obtained for the dynamic model is 7.9 dB, very similar to the 8 dB selected in the design carried out with the resistive model. For other values of α and R_{bat}, the same pattern is found, although for lower R_{bat} the gain margin is always higher.
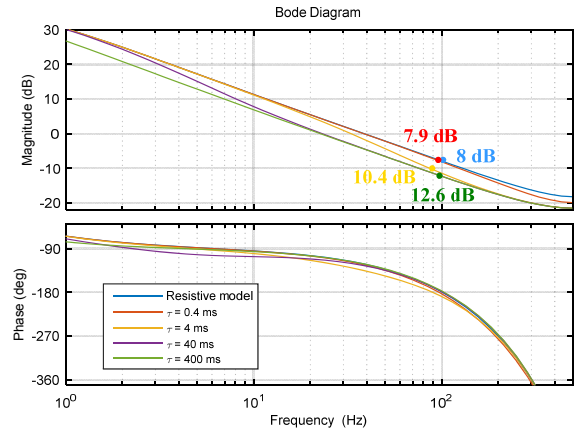

FIGURE 17. Open-loop for parallel impedance emulation, $Y_p \cdot z^{-1} \cdot Z_{vf}$, with R_p = 13.7 mΩ and L_p = 4.35 mH, for different battery parameters: resistive model with R_{bat} = 1 Ω, and dynamic model with R_{bat} = 1 Ω, α = 0.6 and τ = 0.4, 4, 40 and 400 ms.

Concerning the series and parallel impedance emulation, presented in section IV.C, the corresponding open-loop transfer function is $Y_p \cdot z^{-1} \cdot (Z_{vf} + G_{if} \cdot Z_s)$ [see (12) and Fig. 14]. To analyze the stability, its Bode plot is represented in Fig. 18 for R_{bat} = 1 Ω and the same situations as in the previous figure. As can be observed, the gain margins for the dynamic model are always higher than the design gain margin. Furthermore, also in this case, the same pattern is found for other values of α and R_{bat}. As a result, both emulation methods maintain high stability margins for all possible batteries and are thus suitable to be used for universal chargers.
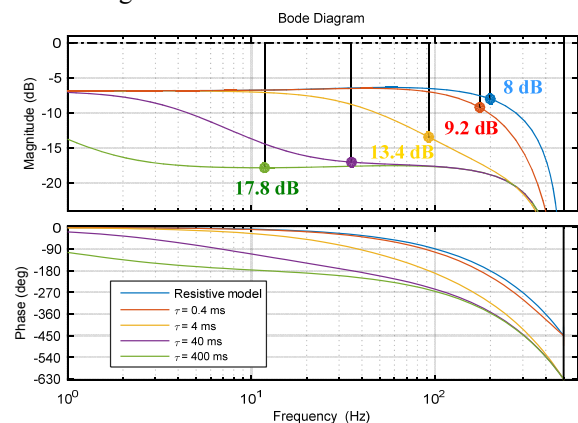

FIGURE 18. Open-loop for the series and parallel impedance emulation, $Y_p \cdot z^{-1} \cdot (Z_{vf} + G_{if} \cdot Z_s)$, with R = 687 mΩ and low-pass filter, for different battery parameters: resistive model with R_{bat} = 1 Ω, and dynamic model with R_{bat} = 1 Ω, α = 0.6 and τ = 0.4, 4, 40 and 400 ms.

V. SIMULATION RESULTS

The battery voltage regulation is tested in this section by using PSIM simulation software. The simulations are carried out in order to compare the following four voltage methods: (i) the traditional control presented in section IV.A; (ii) the parallel impedance emulation method presented in section IV.B, designed as proposed in [40]; (iii) the same method, designed as proposed in this paper; (iv) the series and parallel impedance emulation method proposed in section IV.C.

Each of the voltage regulation methods is simulated for three batteries with different properties. Specifically, their nominal voltage and series resistance are: 48 V − 10 mΩ, 120 V − 100 mΩ, and 240 V − 1 Ω. Figure 19 shows the battery voltage in response to an upward step in the voltage reference so that the charging current increases from 0 to 20 A in all cases. For a better comparison, the battery voltage used in the graphs has been normalized between 0 and 1. As can be observed, the traditional control [Fig. 19(a)] experiences an extremely variable voltage response. The parallel impedance emulation method [Fig. 19(b)] is unstable for $R_{bat,max} = 1\ \Omega$ when designed as proposed in [40], as predicted by the improved model of this paper (see Fig. 8). When designed as proposed in this paper, the parallel impedance emulation method [Fig. 19(c)] becomes stable and fast for the battery resistance range, although a dynamic variation still exists. Finally, the series and parallel impedance emulation method, proposed in this paper [Fig. 19(d)], achieves a voltage response whose dynamics is totally independent of the battery impedance.

The variation in dynamics shown by the traditional control can cause a prolonged battery overvoltage in renewable-energy-based stand-alone systems. To compare the control strategies in this situation, a 20 mΩ battery is connected through the boost converter charger to a PV-based stand-alone system. The simulation results, carried out for an abrupt load disconnection in a situation with high irradiance, are shown in Fig. 20(a) for the traditional control and in Fig. 20(b) for the series and parallel impedance emulation method. At the beginning, the battery voltage is below the maximum value and, as a result, the current reference for CV mode, $I^*_{bat,CV}$, is saturated to the maximum value. Therefore, CC mode is selected and the outer voltage loop is deactivated. Then, after the load disconnection occurs at second 6, the PV power which was consumed by the load is now transferred to the battery, causing the battery current and voltage to increase. At that moment, the voltage control is activated, which makes it possible to reduce the battery charging current and regulate its voltage. As can be observed in Fig. 20(a), the duration of the overvoltage is very long for the traditional control, where the voltage remains 3.1 s over 54.1 V, and is significantly reduced thanks to the proposed method as shown in Fig. 20(b), where the voltage remains 0.5 s over 54.1 V.

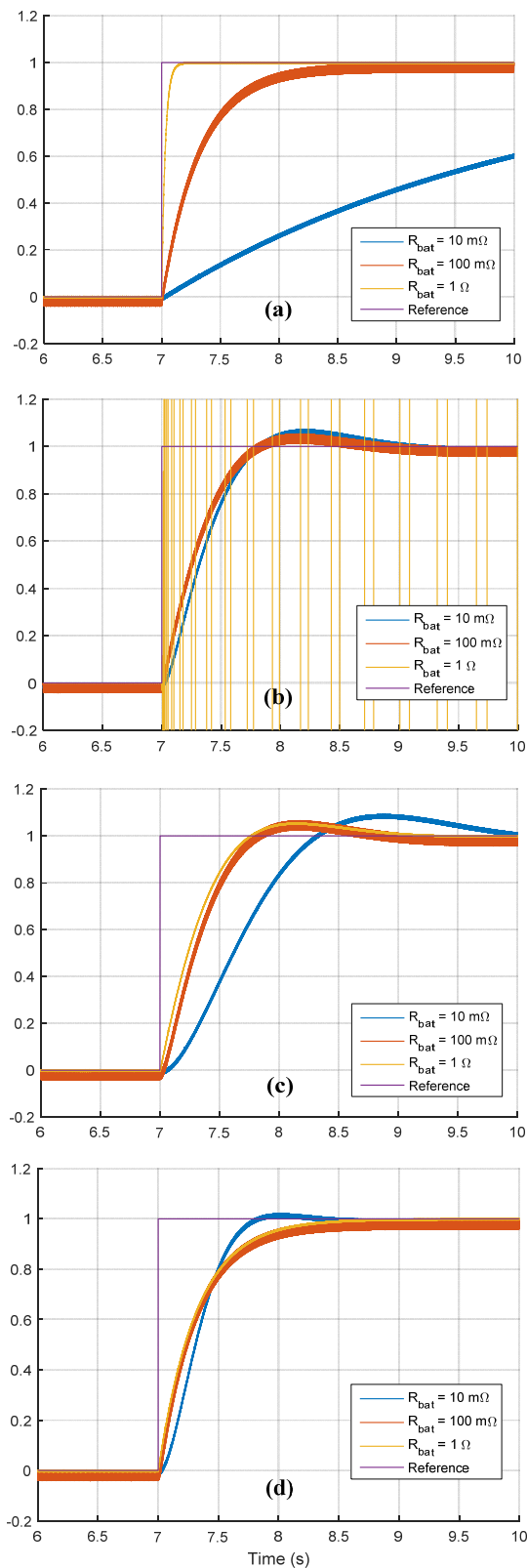**FIGURE 19.** Simulation results of the battery voltage regulation for three different batteries (R_{bat} = 10 mΩ, R_{bat} = 100 mΩ and R_{bat} = 1 Ω): (a) traditional control, (b) parallel impedance emulation method with R_p = 2.26 mΩ, (c) parallel impedance emulation method with R_p = 13.7 mΩ, (d) series and parallel impedance emulation method.
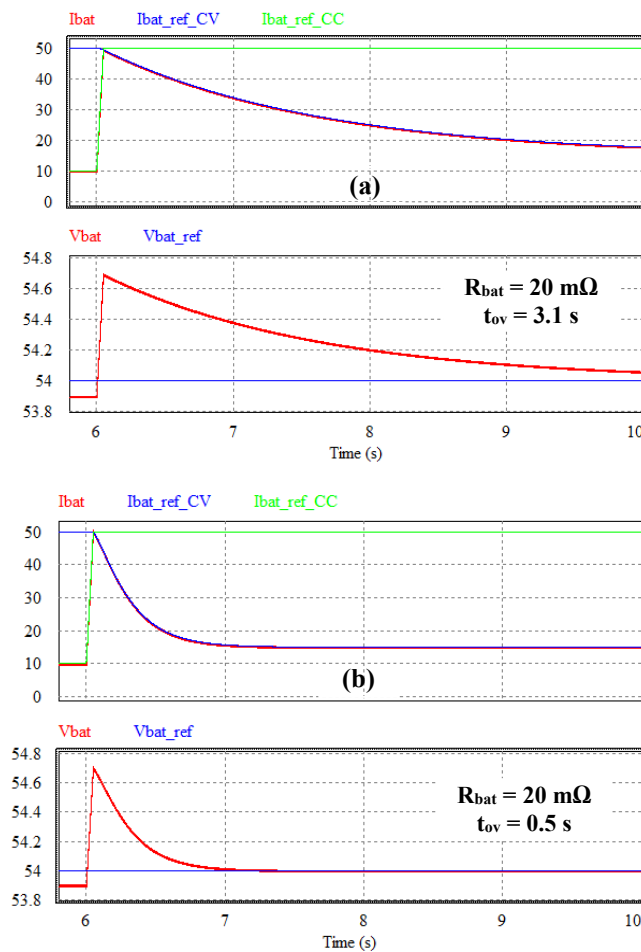
FIGURE 20. Simulation results of the battery voltage regulation after a load disconnection for R_{bat} = 20 mΩ: (a) traditional control, (b) series and parallel impedance emulation method.

VI. CONCLUSION

An effective battery voltage regulation is important to extend the battery lifetime. However, it is difficult to achieve when using universal chargers, since the battery impedance can deviate significantly depending on the battery type, operating point, aging and series-parallel cell connection. As a result, when directly using a PI or integral controller, the control performance may be too far from the desired performance.

In order to reduce the effect of the battery impedance on the voltage regulation, a virtual impedance can be emulated at the battery terminals. In this paper, two methods have been considered, namely parallel impedance emulation, and series-parallel impedance emulation. In both cases, to avoid an unstable emulation near the Nyquist frequency, the design of the virtual impedance must be carried out based on an accurate model, including a discrete analysis of the voltage regulation and an exact model of the current closed-loop.

Although both methods are easy to implement and greatly improve the voltage control performance, the proposed series and parallel impedance emulation is preferred. The reasons

are that it achieves an almost identical voltage response for batteries with impedances in the range of 10 mΩ to 1 Ω and offers better noise immunity.

REFERENCES

[1] A. Aldik, A. T. Al-Awami, E. Sortomme, A. M. Muqbel, and M. Shahidehpour, "A planning model for electric vehicle aggregators providing ancillary services," *IEEE Access*, vol. 6, pp. 70685-70697, Dec. 2018.

[2] C. Wang, B. Huang, and W. Xu, "An integrated energy management strategy with parameter match method for plug-in hybrid electric vehicles," *IEEE Access*, vol. 6, pp. 62204-62214, Nov. 2018.

[3] I.-O. Lee, "Hybrid PWM-resonant converter for electric vehicle on-board battery chargers," *IEEE Transactions on Power Electronics*, vol. 31, no. 5, pp. 3639–3649, May 2016.

[4] X. Lu, Y. Chen, M. Fu, and H. Wang, "Multi-objective optimization-based real-time control strategy for battery/ultracapacitor hybrid energy management systems", *IEEE Access*, vol. 7, pp. 11640-11650, Feb. 2019.

[5] I. de la Parra, J. Marcos, M. García and L. Marroyo, "Control strategies to use the minimum storage requirement for PV power ramp-rate control," *Solar Energy*, vol. 111, pp. 332–343, Jan. 2015.

[6] C. Mateo, J. Reneses, A. Rodriguez-Calvo, P. Frías and A. Sánchez, "Cost-benefit analysis of battery storage in medium-voltage distribution networks," *IET Generation, Transmission & Distribution*, vol. 10, no. 3, pp. 815–821, Feb. 2016.

[7] C.-L. Nguyen, H.-H. Lee and T.-W. Chun, "Cost-optimized battery capacity and short-term power dispatch control for wind farm," *IEEE Transactions on Industry Applications*, vol. 51, no. 1, pp. 595–606, Jan. 2015.

[8] A. Urtasun, P. Sanchis and L. Marroyo, "State-of-charge-based droop control for stand-alone systems with distributed energy storage," *Energy Conversion and Management*, vol. 106, pp. 709–720, Dec. 2015.

[9] A. Urtasun, P. Sanchis, D. Barricarte and L. Marroyo, "Energy management strategy for a battery-diesel stand-alone system with distributed PV generation based on grid frequency modulation," *Renewable Energy*, vol. 66, pp. 325–336, June 2014.

[10] A. Hussain, V.-H. Bui, and H.-M. Kim, "A proactive and survivability-constrained operation strategy for enhancing resilience of microgrids using energy storage systems," *IEEE Access.*, vol. 6, pp. 75495–75507, Dec. 2018.

[11] Y. Han, H. Li, P. Shen, E. A. A. Coelho and J. M. Guerrero, "Review of active and reactive power sharing strategies in hierarchical controlled microgrids," *IEEE Transactions on Power Electronics*, vol. 32, no. 3, pp. 2427–2451, Mar. 2017.

[12] H. Farzin, M. Fotuhi-Firuzabad and M. Moeini-Aghtaie, "A practical scheme to involve degradation cost of lithium-ion batteries in vehicle-to-grid applications," *IEEE Transactions on Sustainable Energy*, vol. 7, no. 4, pp. 1730–1738, Oct. 2016.

[13] B. Zhou, X. Liu, Y. Cao, C. Li, C. Y. Chung and K. W. Chan, "Optimal scheduling of virtual power plant with battery degradation cost," *IET Generation, Transmission & Distribution*, vol. 10, no. 3, pp. 712–725, Feb. 2016.

[14] H. Fang, Y. Wang and J. Chen, "Health-aware and user-involved battery charging management for electric vehicles: linear quadratic strategies," *IEEE Transactions on Control Systems Technology*, vol. 25, no. 3, pp. 911–923, May 2017.

[15] B. Suthar, V. Ramadesigan, S. De, R. D. Braatz and V. R. Subramanian, "Optimal charging profiles for mechanically constrained lithium-ion batteries," *Physical Chemistry Chemical Physics*, vol. 16, no. 1, pp. 277–287, Jan. 2013.

[16] H. A. Catherino, F. F. Feres and F. Trinidad, "Sulfation in lead-acid batteries," *Journal of Power Sources*, vol. 129, no. 1, pp. 113–120, Apr. 2004.

[17] M. J. Isaacson, R. P. Hollandworth, P. J. Giampaoli, F. A. Linkowsky, A. Salim, and V. L. Teofilo, "Advanced lithium ion battery charger," in *15th Annual Battery Conference on Applications and Advances*, pp. 193–198, Jan. 2000.

[18] A. Affani, A. Bellini, G. Franceschini, P. Guglielmi, and C. Tassoni, "Battery choice and management for new-generation electric

vehicles," *IEEE Transactions on Industrial Electronics*, vol. 52, no. 5, pp. 1343–1349, Oct. 2005.

[19] W. G. Hurley, Y. S. Wong, and W. H. Wölfle, "Self-equalization of cell voltages to prolong the life of VRLA batteries in standby applications," *IEEE Transactions on Industrial Electronics*, vol. 56, no. 6, pp. 2115–2120, June 2009.

[20] X. Qu, H. Han, S.-C. Wong, C. K. Tse and W. Chen, "Hybrid IPT topologies with constant current or constant voltage output for battery charging applications," *IEEE Transactions on Power Electronics*, vol. 30, no. 11, pp. 6329–6337, Nov. 2015.

[21] S. Amstrong, M. E. Glavin and W. G. Hurley, "Comparison of battery charging algorithms for stand alone photovoltaic systems," in *2008 Power Electronics Specialists Conference*, pp. 1469–1475, July 2008.

[22] B. J. Huang, P. C. Hsu, M. S. Wu and P. Y. Ho, "System dynamic model and charging control of lead-acid battery for stand-alone solar PV systems," *Solar Energy*, vol. 84, no. 5, pp. 822–830, May 2010.

[23] T. A. Nguyen, X. Qiu, J. D. Guggenberger II, M. L. Crow and A. C. Elmore, "Performance characterization for photovoltaic-vanadium redox battery microgrid systems," *IEEE Transactions on Sustainable Energy*, vol. 5, no. 4, pp. 1379–1388, Oct. 2014.

[24] X. Qiu, T. A. Nguyen, J. D. Guggenberger, M. L. Crow and A. C. Elmore, "A field validated model of a vanadium redox flow battery for microgrids," *IEEE Transactions on Smart Grids*, vol. 5, no. 4, pp. 1592–1601, July 2014.

[25] N. Tashakor, E. Farjah and T. Ghanbari, "A bi-directional battery charger with modular integrated charge equalization circuit," *IEEE Transactions on Power Electronics*, vol. 32, no. 3, pp. 2133–2145, Mar. 2017.

[26] P.-J. Liu and C.-H. Yen, "A fast charging switching-based charger with adaptive hybrid duty cycle control for multiple batteries," *IEEE Transactions on Power Electronics*, vol. 32, no. 3, pp. 1975–1983, Mar. 2017.

[27] R. J. Wai and S. J. Jhung, "Design of energy-saving adaptive fast-charging control strategy for Li-FePO$_4$ battery module," *IET Power Electronics*, vol. 5, no. 9, pp. 1684–1693, Nov. 2012.

[28] A. M. A. Haidar and K. M. Muttaqi, "Behavioral characterization of electric vehicle charging loads in a distribution power grid through modeling of battery chargers," *IET Transactions on Industry Applications*, vol. 52, no. 1, pp. 483–492, Jan. 2016.

[29] P. H: V. Quang, T. T. Ha and J.-W. Lee, "A fully integrated multimode wireless power charger IC with adaptive supply control and built-in resistance compensation," *IET Transactions on Industrial Electronics*, vol. 62, no. 2, pp. 1251–1261, Feb. 2015.

[30] S. G. Tesfahunegn, O. Ulleberg, T. M. Undeland and P. J. S. Vie, "A simplified battery charge controller for safety and increased utilization in standalone PV applications," in *37th IEEE Photovoltaic Specialists Conference*, pp. 2441–2447, June 2011.

[31] D. Pavkovic, M. Lobrovic, M. Hrgetic, A. Komljenovic and V. Smetko, "Battery current and voltage control system design with charging application," in *2014 IEEE Conference on Control Applications*, pp. 1133–1138, Oct. 2014.

[32] S. Biswas, L. Huang, V. Vaidya, K. Ravichandran, N. Mohan and S. V. Dhople, "Universal current-mode control schemes to charge Li-ion batteries under DC/PV source," *IEEE Transaction on Circuits and Systems–I: Regular Papers*, vol. 63, no. 9, pp. 1531–1542, Sep. 2016.

[33] A. A.-H. Hussein and I. Batarseh, "A review of charging algorithms for nickel and lithium battery chargers," *IEEE Transactions on Vehicular Technology*, vol. 60, no. 3, pp. 830–838, Mar. 2011.

[34] H. Rahimi-Eichi and M.-Y. Chow, "Adaptive parameter identification and state-of-charge estimation of lithium-ion batteries," in *38th IEEE Industrial Electronics Society Conference*, pp. 4012–4017, Oct. 2012.

[35] H. M. O. Filho, D. S. Oliveira and C. E. Alencar e Silva, "Three-stage static power converter for battery charging feasible for small wind energy conversion systems," *IEEE Transactions on Industry Applications*, vol. 50, no. 5, pp. 3602–3610, Sep. 2014.

[36] Y.-D. Lee and S.-Y. Park, "Rapid charging strategy in the constant voltage mode for a high power Li-ion battery," in *2013 IEEE Energy Conversion Congress and Exposition*, pp. 4725–4731, Sep. 2013.

[37] A. Urtasun, P. Sanchis, and L. Marroyo, "Frequency-based energy-management strategy for stand-alone systems with distributed battery storage," *IEEE Transactions on Power Electronics*, vol. 30, no. 9, pp. 4794–4808, Sept. 2015.

[38] J. Jiang, C. Zhang, J. Wen, W. Zhang and S. M. Sharkh, "An optimal charging method for Li-ion batteries using a fuzzy-control approach based on polarization properties," *IEEE Transactions on Vehicular Technology*, vol. 62, no. 7, pp. 3000–3009, Sep. 2013.

[39] P. Albertos, A. Sala and M. Olivares, "Fuzzy logic controllers. Methodology, advantages and drawbacks," in *Congreso Español sobre Tecnologías y Lógica Fuzzy*, Dec. 2000.

[40] A. Urtasun, A. Berrueta, P. Sanchis, and L. Marroyo, "Parameter-independent control for battery chargers based on virtual impedance emulation," *IEEE Transactions on Power Electronics*, vol. 33, no. 10, pp. 8848–8858, Oct. 2018.

[41] U. Westerhoff, K. Kurbach, F. Lienesch, and M. Kurrat, "Analysis of lithium-ion battery models based on electrochemical impedance spectroscopy," *Energy Technology*, vol. 4, no. 12, pp. 1620–1630, Dec. 2016.

[42] A. Berrueta, A. Urtasun, A. Ursúa, and P. Sanchis, "A comprehensive model for lithium-ion batteries: from the physical principles to an electrical model," *Energy*, vol. 144, pp. 286–300, Feb. 2018.

[43] X. Zhang, Y. Wang, D. Yang, and Z. Chen, "An on-line estimation of battery pack parameters and state-of-charge using dual filters based on pack model," *Energy*, vol. 115, pp. 219–229, Nov. 2016.

[44] S.-Y. Cho, I.-O. Lee, J.-I. Baek and G.-W. Moon, "Battery impedance analysis considering DC component in sinusoidal ripple-current charging," *IEEE Transactions on Industrial Electronics*, vol. 63, no. 3, pp. 1561–1573, Mar. 2016.

[45] M. Einhorn, F. V. Conte, C. Kral and J. Fleig, "Comparison, selection and parameterization of electrical battery models for automotive applications," *IEEE Transactions on Power Electronics*, vol. 28, no. 3, pp. 1429–1437, Mar. 2013.

[46] N. Somakettarin and T. Funaki, "Parameter extraction and characteristics study for manganese-type lithium-ion battery," *International Journal of Renewable Energy Research*, vol. 5, no. 2, pp. 464–475, June 2015.

[47] Y. Jing, W. Xuezhe, D. Haifeng, Z. Jiangong and X. Xudong, "Lithium-ion battery internal resistance model based on the porous electrode theory," in *2014 IEEE Vehicle Power and Propulsion Conference*, pp. 1–6, Oct. 2014.

[48] J. D. Dogger, B. Roossien and F. D. J. Nieuwenhout, "Characterization of Li-ion batteries for intelligent management of distributed grid-connected storage," *IEEE Transactions on Energy Conversion*, vol. 26, no. 1, pp. 256–263, Mar. 2011.

[49] S. Schaeck, A. O. Stoermer, F. Kaiser, L. Koehler, J. Albers and H. Kabza, "Lead-acid batteries in micro-hybrid applications. Part I. Selected key parameters," *Journal of Power Sources*, vol. 196, no. 3, pp. 1541–1554, Feb. 2011.

[50] T. Dragicevic, J. M. Guerrero, J. C. Vasquez, and D. Skrlec, "Supervisory control of an adaptive-droop regulated DC microgrid with battery management capability," *IEEE Transactions on Power Electronics*, vol. 29, no. 2, pp. 695–706, Feb. 2014.

[51] J. L. Agorreta, M. Borrega, J. López, and L. Marroyo, "Modeling and control of N-paralleled grid-connected inverters with LCL filter coupled due to grid impedance in PV plants," *IEEE Trans. Power Electron.*, vol. 26, no. 3, pp. 770–785, 2011.

[52] M. Sitbon, S. Schacham, and A. Kuperman, "Disturbance observer-based voltage regulation of current-mode-boost-converter-interfaced photovoltaic generator," *IEEE Trans. Ind. Electron.*, vol. 62, no. 9, pp. 5776–5785, 2015.